ANNALS OF GEOPHYSICS, 68, 5, DM578, 2025; doi:10.4401/ag-9305
OPEN ACCESS

The OTRIONS seismic network: instrumentation upgrade and borehole installation

Andrea Tallarico[1,2], Domenico Patella[1], Teresa Ninivaggi[*,3], Giuseppe Ruzza[3], Gianpaolo Cecere[3], Marilena Filippucci[1,2], Giulio Selvaggi[2]

(1) University of Bari Aldo Moro, Department of Earth and Geo-Environmental Science, Bari, Italy
(2) Istituto Nazionale di Geofisica e Vulcanologia, ONT, Roma, Italy
(3) Istituto Nazionale di Geofisica e Vulcanologia, Sezione Irpinia, Grottaminarda, Italy

Article history: received March 8, 2025; accepted October 21, 2025

Abstract

The Gargano Promontory is one of the most seismically active regions of southern Italy. Here we installed the OTRIONS seismic network consisting, at its very beginning, of 12 short period stations. The network has operated in this region since 2013, and it has been upgraded during time. Five out of these stations have been equipped with broadband sensors. More recently, we installed a posthole seismometer at the site of Lucera at a depth of 30 meters to further reduce seismic noise. In this paper, we describe the OTRIONS network upgrade and focus basic guidelines for the installation of a borehole seismometer. We have performed a post-installation orientation considering both the polarization analysis and the correlation of seismic recordings because of the impossibility of a mechanical orientation of the sensor that rotated during the descent phase. Both methods give coherent results. We have also analysed the noise level after the station's upgrade. The maintenance and upgrade of the seismic network is fundamental for the continuous monitoring of this area.

Keywords: OTRIONS Seismic Network; Gargano Promontory; Borehole Installation; Seismometer Orientation; Background Seismic Noise

1. Introduction

The Apulian region (SE Italy) represents the foreland sector of the Southern Apennines and is essentially composed of three carbonate plateaus (Ricchetti et al., 1988). The northernmost plateau constitutes the Gargano Promontory (GP). The GP is bounded by an alluvial plain named Tavoliere to the south, and by a mountainous region to the west, the Dauno Sub-Apennine (Pieri et al., 1997). These areas represent the most seismically active zones of the Apulia region, with several earthquakes of Mw > 5.0 in the past centuries (Del Gaudio et al., 2007). Given the absence of medium to strong earthquakes for centuries and the intense micro-seismicity recorded in this area in the last decade (Miccolis et al., 2021), the continuous seismic monitoring and the upgrading of seismic stations are of fundamental importance to understand the present dynamics of the area. The OTRIONS (multi-parametric network for the study and monitoring of natural hazards in the OTRanto channel and IONian Sea) project was funded in 2013, in the context of the "European Territorial Cooperation Programme Greece-Italy 2007-2013" (INTEREG III). One of the goals of this project was to deploy a local seismic network around the GP

(Tallarico, 2015). The OTRIONS seismic network (hereafter called with the FDSN code OT, University of Bari "Aldo Moro", 2013) changed its configuration and the number of recording stations during the last twelve years, as detailed by Filippucci et al. (2021), both for improving the network coverage and for technical and logistical reasons. Two new seismic stations (OT16 and OT17) were added in 2021. To detect possible electromagnetic signals related to seismic activity in GP, the station OT04 hosts additionally a magnetotelluric sensor from September 2021 onwards (Ventola et al., 2024). Station location and equipment with the corresponding operation periods are reported in Table 1 and shown in Fig. 1.

The OT network was initially composed of 12 three component seismic stations named sequentially from OT01 to OT12. Each seismic station was equipped with a short-period Lennartz 3D-V seismometer and a Sara SL06 data-logger. Stations TAR1 and CGL1 are equipped with Nanometrics instruments (Trillium Compact 120s and Taurus). Today 16 seismic stations (CGL1, MASS, OT03, OT04, OT05, OT06, OT07, OT11, OT12, OT13, OT14, OT15, OT16, OT17, OTP1 and TAR1) are operating across the Apulian territory (University of Bari – Aldo Moro, 2013, https://eida.ingv.it/it/network/OT).

Five of these stations (OT05, OT11, OT12, OT14, OT16) were upgraded in February 2024 with broadband instruments. Additionally, a borehole station (OTP1) has also been installed in the same OT11 seismic site, in the Technical, Economic and Technological High School "Vittorio Emanuele III", at Lucera (FG). The town of Lucera is in the Tavoliere plain, a foredeep filled by sediments (Casnedi, 1988) and placed between the Apulia foreland and the Dauno Sub-Apennine chain (Patacca and Scandone, 2004). This transitional geodynamic context makes the Lucera site particularly significant for studies on crustal structure and site effects. In fact, the Lucera seismic station (OTP1 and OT11) can be used to study the effects of the Tavoliere sedimentary basin on the propagation of seismic waves for hazard purpose, due to amplification and resonance phenomena that can be evaluated by good quality broad-band and accelerometric signals (Wirth et al., 2019). The underlying Apulian foreland is instead characterized by a rigid carbonate platform that can act as a regional reference for the bedrock (Amato et al., 2014). Furthermore, the proximity of the Lucera site to the Sub-Apennine chain, more tectonically complex than the Apulian foreland (Di Bucci and Mazzoli, 2002), offers an ideal geologic contrast that would allow to examine lateral heterogeneities in the crustal structure and their influence on the seismic response.

In this paper we provide a detailed description of the upgrading of the five seismic stations and the working steps for the borehole installation. As the posthole sensor has rotated around a vertical axis during the descent phase, we have calculated the orientation of the two horizontal components of the seismic station. We also show the level of the background seismic noise recorded after upgrading the five sensors.

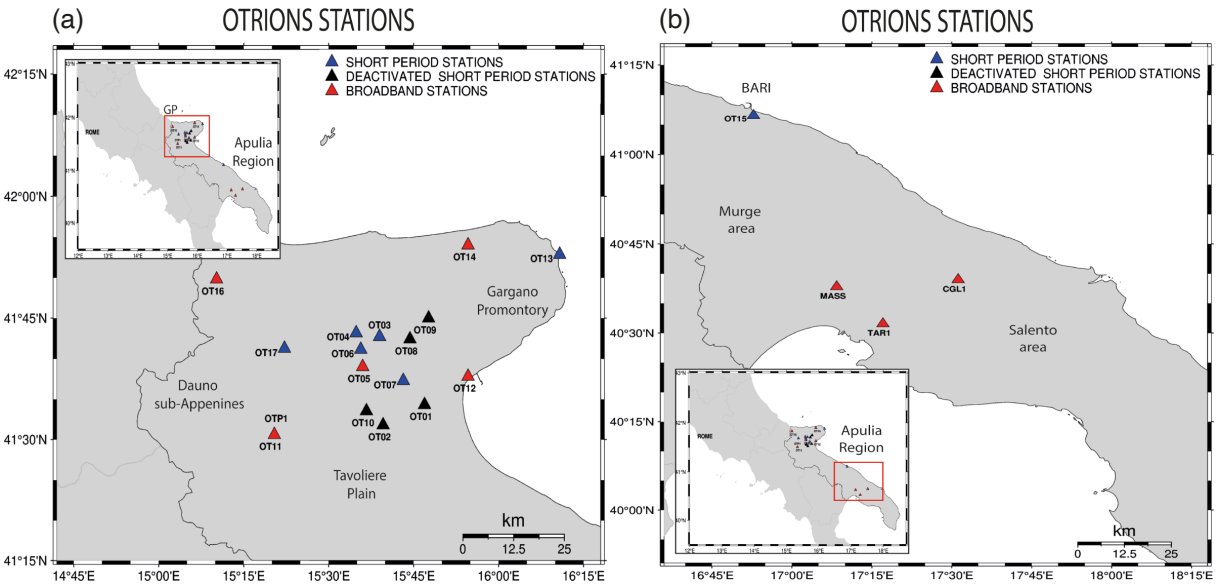

Figure 1. The OT seismic stations (triangles). (a) OT stations located in northern Apulia and (b) stations of central and southern Apulia. Blue triangles are stations with short-period sensor equipment; the black ones are those with short period seismometers deactivated over the years; the red triangles are stations with broadband sensors. Details of instruments and period of operation are in Table 1.

Table 1. List of the OT network stations with details: name (FDSN code), location (Municipality), geographic coordinates (Latitude N and Longitude E in decimal degrees, Elevation (m) above the sea level); type of seismometer (Sensor and Sensitivity); type of Data Logger; characteristics of the sensor installation site (Housing type); period of acquisition with data available in local mode (Start and End Operation); acquisition period with data available on EIDA (Start and End Operation, EIDA). All stations sample at a rate $\Delta T = 10$ ms (sps = 100 Hz). Grey rows correspond to the deactivated stations.

FDSN code	Municipality	Latitude N	Longitude E	Elevation (m)	Sensor	Sensitivity	Data Logger	Housing Type	Start Operation	End Operation	Start Online (EIDA)	End Online (EIDA)
CGL1	Ceglie Messapica (BR)	40.648	17.517	303	Trillium Compact 120s	1.50E+03	Nanometrics Taurus	Inside Building	2016-11-08 T15:01:10	~	2019-05-16 T12:03:03	~
MASS	Massafra (TA)	40.633	17.144	274	Trillium Compact 120s	7.49E+02	Nanometrics Taurus	Inside Building	2013-10-18 T12:26:46	~	2019-05-16 T11:59:46	~
OT01	Monte Aquilone – Manfredonia (FG)	41.572	15.782	128	LE-3D lite 1s	1.68E+09	SARA SL06	Manhole	2013-02-18 T10:21:24	2013-10-25 T08:59:11	~	~
OT02	ss89 km – Private Address – San Giovanni Rotondo (FG)	41.530	15.660	100	LE-3D lite 1s	1.68E+09	SARA SL06	Manhole	2013-04-22 T11:41:46	2014-08-15 T23:20:32	~	~
OT03	Civil Protection – San Marco in Lamis (FG)	41.712	15.650	655	LE-3D lite 1s	1.68E+09	SARA SL06	Manhole	2013-04-22 T13:47:06	~	2019-05-16 T10:46:32	~
OT04	Stignano – San Marco in Lamis (FG)	41.720	15.581	279	LE-3D lite 1s	1.68E+09	SARA SL06	Manhole	2013-04-30 T16:29:05	~	2019-05-16 T10:53:22	~
OT05	Rignano Garganico (FG)	41.659	15.603	180	LE-3D lite 1s	1.68E+09	SARA SL06	Manhole	2013-04-22 T11:41:48	2024-02-20 T10:00:00	2019-05-16 T10:56:00	2024-02-20 T10:00:00
					Trillium Compact 20s	3.01E+08	Nanometrics Centaurus	~	2024-02-20 T10:00:00	~	2024-02-20 T10:00:00	~
OT06	Rignano Garganico (FG)	41.686	15.594	584	LE-3D lite 1s	1.68E+09	SARA SL06	Manhole	2013-04-18 T13:32:05	~	2019-05-16 T10:58:15	~
OT07	San Giovanni Rotondo (FG) – Pozzo Costarelle	41.621	15.719	154	LE-3D lite 1s	1.68E+09	SARA SL06	Manhole	2013-04-29 T11:08:09	~	2019-05-16 T11:01:11	~
OT08	San Giovanni Rotondo (FG) – Cimitero	41.621	15.719	154	LE-3D lite 1s	1.68E+09	SARA SL06	Manhole	2013-04-18 T16:32:05	2015-05-18 T00:00:03	~	~
OT09	Caserma Guardaboschi – San Giovanni Rotondo (FG)	41.75	15.794	846	LE-3D lite 1s	1.68E+09	SARA SL06	Manhole	2013-04-22 T11:44:36	2015-09-22 T00:00:01	~	~

FDSN code	Municipality	Latitude N	Longitude E	Elevation (m)	Sensor	Sensitivity	Data Logger	Housing Type	Start Operation	End Operation	Start Online (EIDA)	End Online (EIDA)
OT10	Borgo Arpinova (FG)	41.559	15.611	64	LE-3D lite 1s	1.68E+09	SARA SL06	Manhole	2013-04-18 T13:32:04	2018-12-20 T00:00:00	~	~
OT11	Lucera (FG)	41.515	15.336	215	LE-3D lite 1s	1.68E+09	SARA SL06	Manhole	2013-04-29 T09:17:20	2024-03-11 T11:05:00	2019-05-16 T11:50:53	2024-03-04
					Trillium Compact 120s	4.07E+06	Nanometrics Accelerometer	~	2024-03-11 T11:05:00	~	2024-03-11 T11:05:00	~
					Titan Accelerometer	2.99E+08	Nanometrics Centaurus	~	2024-03-11 T11:05:00	~	2024-03-11 T11:05:00	~
OTP1					Nanometrics T120-PostHole3	4.77E+09	Nanometrics Centaurus	30 m depth well	2024-04-18 T18:00:00	~	2024-04-18 T18:00:00	~
OT12	Manfredonia (FG)	41.632	15.908	30	LE-3D lite 1s	1.68E+09	SARA SL06	Manhole	2013-04-18 T13:32:03	2024-02-15 T17:00:00	2019-05-16 T11:54:49	2024-02-15 T17:00:00
					Trillium Compact 20s	3.01E+08	Nanometrics Centaurus	~	2024-02-15 T17:00:00	~	2024-02-15 T17:00:00	~
OT13	Vieste (FG)	41.881	16.1791	0	LE-3D lite 1s	1.68E+09	SARA SL06	Manhole	2015-06-12 T11:44:14	~	2019-05-16 T11:53:09	~
OT14	Ischitella (FG)	41.897	15.907	0	LE-3D lite 1s	1.68E+09	SARA SL06	Manhole	2015-06-22 T11:49:00	2024-02-15 T17:00:00	2019-05-16 T11:54:49	2024-02-15 T17:00:00
					Trillium Compact 20s	3.01E+08	Nanometrics Centaurus	~	2024-02-15 T17:00:00	~	2024-02-15 T17:00:00	~
OT15	Bari (BA)	41.109	16.880	0	LE-3D lite 1s	1.68E+09	SARA SL06	Basement	2018-03-12 T11:20:10	~	2019-05-16 T11:56:42	~
OT16	Chieuti (FG)	41.834	15.170	256	LE-3D lite 1s	1.68E+09	SARA SL06	Manhole	2021-04-14 T08:42:57	2024-02-28 T08:42:00	2021-04-14 T08:42:57	2024-02-28 T08:42:00
					Trillium Compact 20s	3.01E+08	Nanometrics Centaurus	~	2024-02-28 T08:42:00	~	2024-02-28 T08:42:00	~
OT17	San Severo (FG)	41.688	15.370	91	LE-3D lite 1s	1.68E+09	SARA SL06	Manhole	2021-09-06 T09:26:05	~	2021-09-06 T09:26:05	~
TAR1	Taranto	40.526	17.285	140	Trillium 40s	1.50E+09	Nanometrics Taurus	Manhole	2016-01-11 T13:17:00	~	2019-05-16 T11:56:42	~

2. Network upgrade

2.1 Installation of five broadband surface stations

The seismic stations OT05, OT11, OT12, OT14, OT16 have been completely renewed at the beginning of 2024 by through replacement of both the sensor and the data logger. The Lennartz 3D 1 s seismometers and the Sara SL06 data loggers have been replaced by the Nanometrics Trillium Compact 20 s and the Nanometrics Centaur data-logger. All the stations are housed in a manhole thermally insulated by a 10 cm thick layer of polystyrene that covers the walls and top of the manhole. As indicated in Table 1, some sensors are inside buildings. Stations are powered by the city power supply where available, otherwise by a solar panel. Only the station OT05, which is exposed to the sun all day, is equipped with a cooling system, consisting of two fans controlled by a thermostat, operating when the temperature inside the cabinet reaches 25 °C. To evaluate the noise of the cooling system on the recordings, we analysed the PPSDs for two different periods: during summer, when the cooling system is on, and during winter, when the cooling system is off. Results are described in Section 3 and indicate that the cooling system does not affect the quality of the recordings. Figure 2 shows the OT05 station. The update interventions took place during February and March 2024.

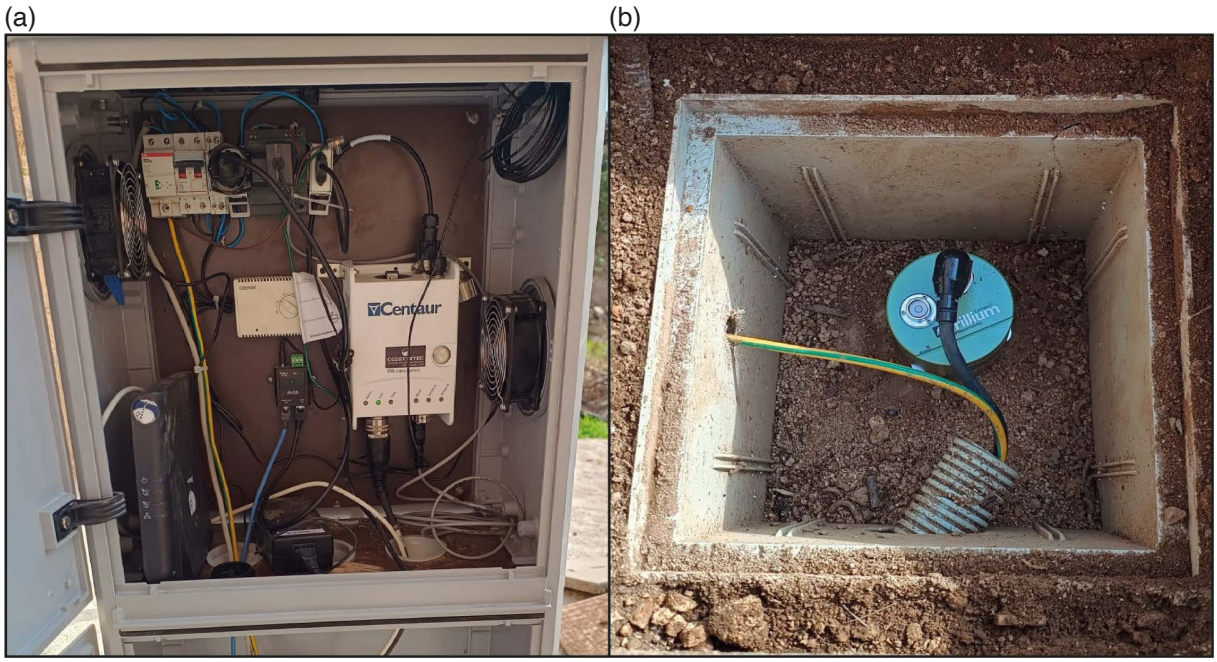

Figure 2. The OT05 station. (a) Internal part of the plastic cabin which contains the new Centaur data logger. (b) The Trillium Compact 20s.

In the city of Lucera (FG), OT11 has been upgraded by the replacement of the surface instrumentation as the station in Fig. 2. In addition, a Nanometrics Titan TACCL-N1 accelerometer has been installed into a 70 cm depth vault made by a concrete sump (Table 1).

To provide better protection against water and temperature changes, the internal parts of both concrete sumps were covered by a 10 cm thick polystyrene (Fig. 3a-b). The concrete sumps are linked through underground plastic pipes which contain sensor cables (Fig. 4). A cabin was used to host other components and protect them against major weather events. As shown in Fig. 3b, the cabin contain:

- Nanometrics Centaur data-loggers;
- GPS antennas;
- Emergency battery charged through the nearby school electrical system;
- Satellite router;
- LTE modem;
- Internet switch.

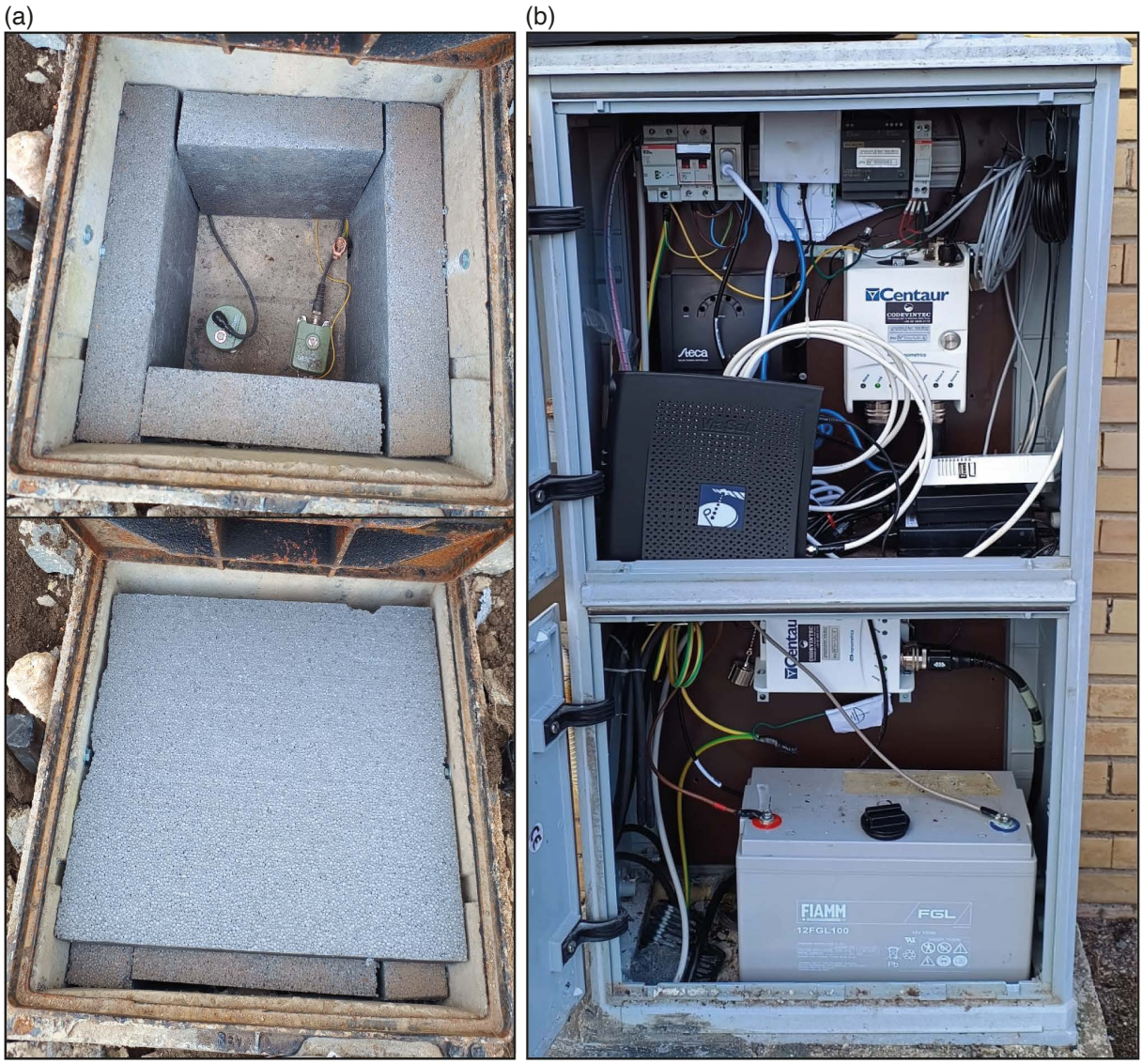

Figure 3. The seismic station OT11. (a) Concrete manhole with thermo-insulating cover in polystyrene. (b) Plastic cabin containing data loggers.

2.2 The borehole station OTP1

The installation of a borehole seismometer at a depth of 30 m (Nanometrics Trillium T120-PH3) has been designed in the same location of OT11 (Lucera). This station is named OTP1. One of the main reasons for installing a seismometer in a borehole is to reduce the background seismic noise, obtaining a better signal-to-noise ratio. Noise signals induced by human activities, wind and/or temperature changes, limit the capacity to resolve high-frequency signals generated by earthquakes (Hutt et al., 2017). The installation procedure consists of three steps:

1) the drilling and the installation of the steel casing;
2) the sensor installation;
3) the computation of the azimuthal direction of the horizontal components.

2.2.1 Steel pipes installation

The T120-PH3 can self-level if the borehole is within 5 degrees with respect to the true vertical. Since achieving perfect verticality in boreholes is technically challenging, we opted to drill a hole with a larger diameter than the steel

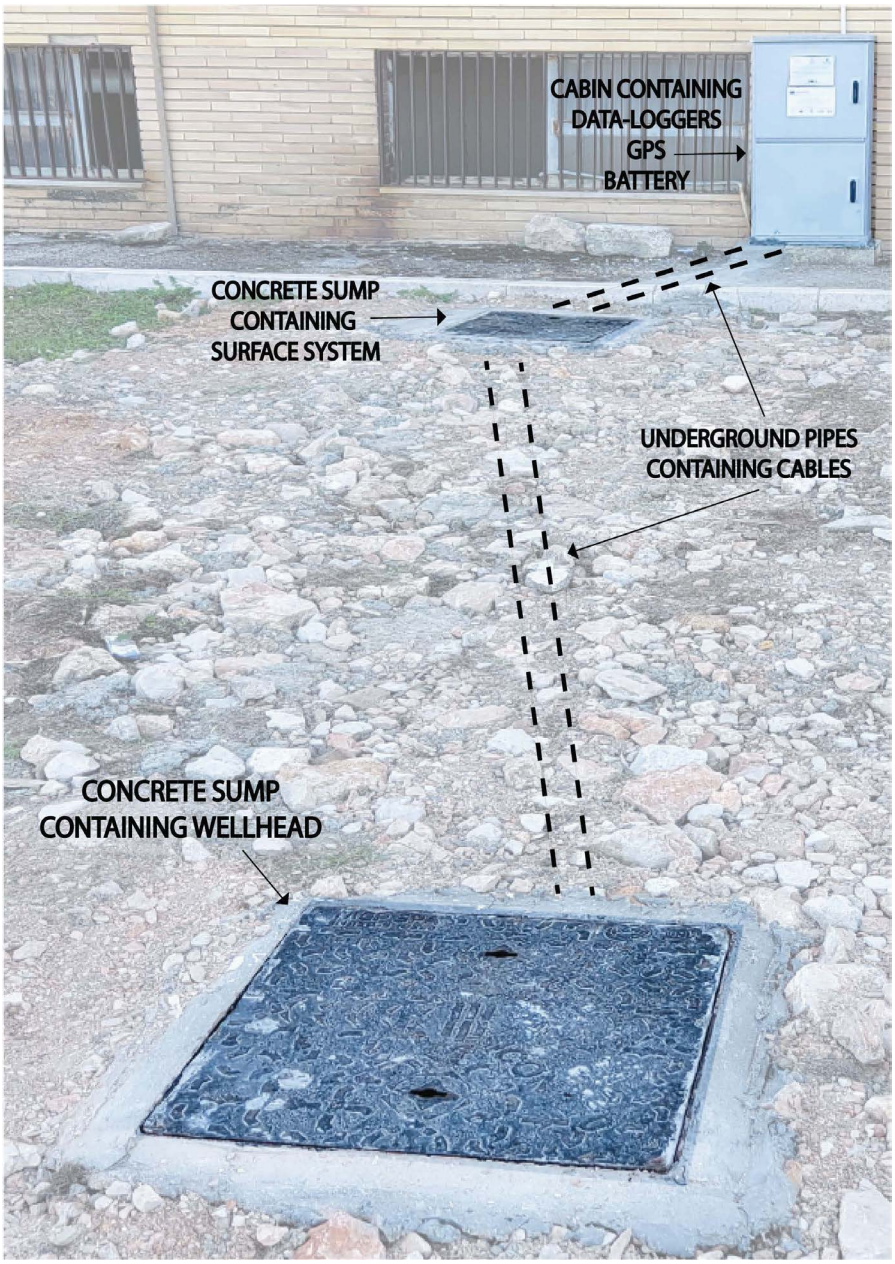

Figure 4. General scheme of both surface and well manholes connected to the data logger cabin.

casing. This approach provided useful additional space to optimize the vertical installation of the steel casing, consisting of six 5 m segments (Fig. 5).

The first phase began with the well drilling (Fig. 6a). To choose the drill site, we had to consider that the sensor is equipped with a 40-meter cable for power and data transmission, forcing the wellhead to be within 10 m from the cabin that houses the datalogger. The drilling started in March 2024 (Fig. 6a) and reached the depth of 31 meters within a couple of days. During the operations, wet clayey and sandy materials were encountered. In fact, this region belongs to the Northwestern Tavoliere which is characterized by porous aquifers with a piezometric level equal to −10.49 m (Di Nunno and Granata, 2020) compatible with our drilling observations. The drill bit was 35 cm large, while the adopted steel casing had an external diameter of 16.4 cm.

Once the hole was completed, the first segment of the steel pipe was lowered into the hole, sealed with steel plate welded to the base to prevent water infiltration. Two successive casing segments were welded (Fig. 5b) before the descent, making the junction resistant and ensuring the straight condition of the resulting pipe (Fig. 6b-c-d).

The last segment was equipped with a metal handle (Fig. 6e) to facilitate the control of the entire tube. Using the drilling machine, the operators were able to keep the steel casing lifted from the bottom; the tube

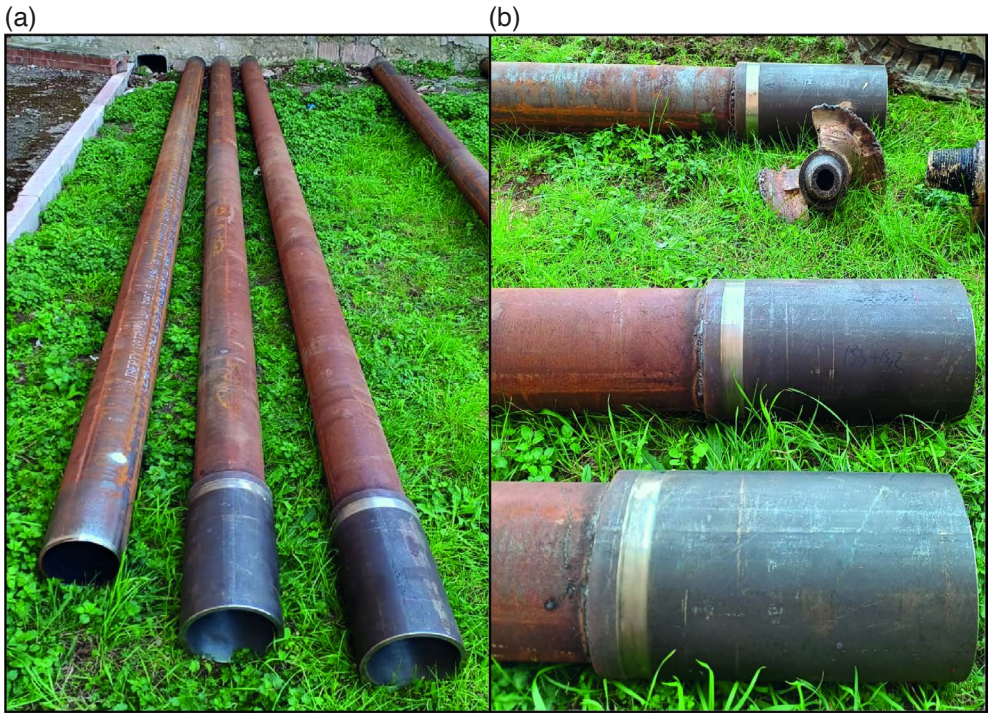

Figure 5. (a) Segments of the steel pipe. (b) Details of welded joints used to join different pipe segments.

Figure 6. (a) Drilling operation of the well. (b) Phase of lifting and alignment of one of the steel pipe segments. (c-d) welding process to join two segments through the external steel joint and result. (e) Pouring liquid cement into the space between rocks and the external side of the pipe.

acts as a pendulum, achieving a condition of perfect verticality. At this stage, construction breach was poured into the hole until a solid base was created at the desired depth (around 30 m) and the space between the casing and the surrounding rocks was partially filled.

To guarantee a perfect coupling, liquid cement was prepared and poured into the breach related voids (Fig. 6e). The pipe was then blocked at the surface allowing the cement to dry prior to the sensor installation.

2.2.2 Posthole sensor installation

The Trillium T120-PH3 was equipped with a steel cable, cable ties, and cable clamps.

In addition, other components were necessary to perform a complete installation: copper sand (sold as abrasive sand for sandblasting), wellhead cap, concrete sump with cap.

The sensor was lowered by hand with the help of four people, but first the communication between the sensor and the datalogger was successfully tested.

At the top of the sensor there is a metal ring for fixing the steel cable and next to it there is the sensor cable connector. It was essential that the sensor cable remained free from tension caused by the weight of the sensor. To achieve this, cable ties were mounted along the steel cable, the first one at 1 m from the sensor and then every 10 m. This type of fastening allowed to release the tension exclusively on the steel cable keeping the sensor cable freer (Fig. 7a).

At the inner bottom of the steel casing a 4 cm thick sand layer was poured according to the sensor user manual before gently lowering the sensor. To ensure the sensor reached the bottom some coloured tape was placed on the sensor cable every 10 m which helped track the distance travelled by the sensor and attention was paid to the release of the tension that may cause visible deformations on the steel cable proving the release of the weight.

Figure 7. (a) Details of the cable ties during the descent of the sensor into the steel casing. (b) Steel cap that supports the cable ties for the data cable and the lifting cable.

Once the tension of the steel cable with the sensor housed at the bottom was ensured, more copper sand was poured into the tube until the sensor was completely covered. The volume of sand needed had been calculated in a previous step, knowing the dimensions of the sensor and the steel casing. We used copper slag because unlike sand it does not tend to cement even in the absence of water, ensuring the recovery of the sensor in the future.

The wellhead was then closed to create a stable support for the sensor lifting cable clamps. A specific metal cap was designed, paying attention to the sensor cable connectors which are larger in diameter than the cable itself (Fig. 7b). Finally, silicone sealant was used to provide additional protection against water infiltration and manhole made by concrete with a cast iron cap were installed to protect the manhole-head. A general scheme of the manhole system is shown in Fig. 8.

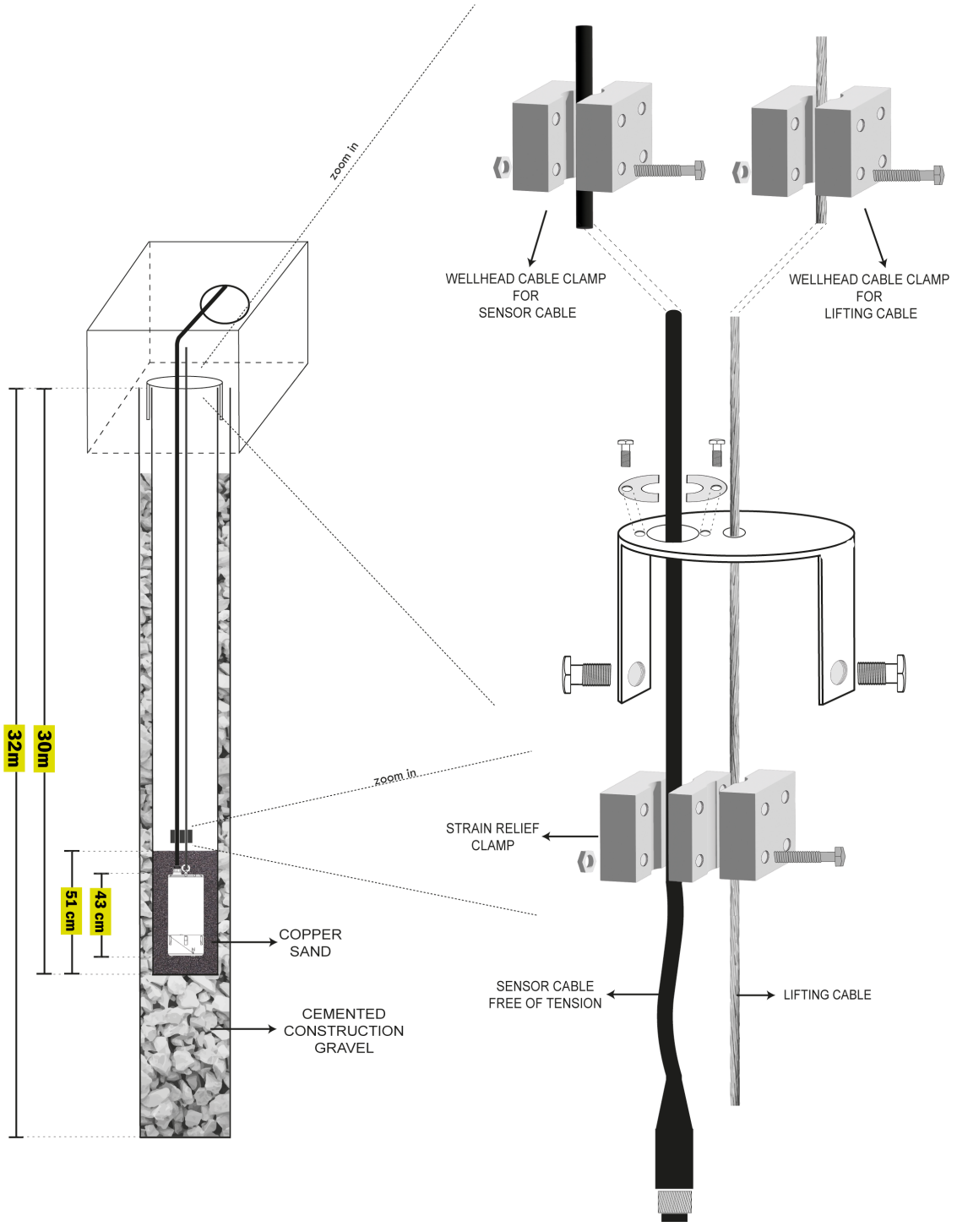

Figure 8. Features of the well system.

3. The orientation of the post-hole seismometer

The orientation of the two horizontal components of the seismic station OTP1 is unknown, as the seismometer has rotated around the vertical axis during the descent phase in the borehole.

There are two standard methods to determine the azimuthal direction angle θ_{az} of horizontal components of seismometers: (1) exploiting the particle motion of seismic waves, as the vibration of direct P-waves in the radial direction (e.g. Aster and Shearer, 1991; Zheng and McMechan, 2006), or exploiting the radial-vertical displacement induced by surface waves (e.g. Ekström and Busby, 2008) extracted also from ambient seismic noise (e.g. Zha et al., 2013); (2) maximizing the cross-correlation between horizontal traces recorded by adjacent sensor pairs (e.g. Stabile et al., 2020; Zheng and McMechan, 2006).

We have applied the two methods, analysing the polarization of direct P-waves of earthquake recordings and maximizing the correlation between the posthole horizontal components of OTP1 and those of reference station OT11. To select the earthquakes with good quality signals, we have visually inspected the recordings of local, regional and teleseismic earthquakes with magnitude greater than 3.0, 4.5, 6.0, respectively, which occurred since the station installation from March 2024 up to February 2025. Among these earthquakes, we have selected the earthquakes listed in Table 2, which show high quality recorded signals, and therefore, allow a good estimate of the angle θ_{az}.

Table 2. Earthquakes list.

Event ID	Time (UTC)	Latitude N	Longitude E	Depth (km)	Magnitude	Description
39152781	2024-06-11T19:08:25	38.05	21.76	17.8	mb 4.7	Greece
39587121	2024-07-06T17:34:32	37.9	21.13	21.1	Mwp 5	Ionian Greek Coast
40017741	2024-08-10T03:28:33	47.09	144.8	404.3	Mwp 6.4	Russia [Sea]
39998581	2024-08-08T07:42:54	31.68	131.5	8.6	Mwp 7.1	Kyushu, Japan [Sea]
40652331	2024-10-16T07:46:33	38.35	38.8	8.6	Mwp 6.1	Turkey
40655961	2024-10-16T18:56:49	36.41	70.73	164.8	Mwp 6	Afghanistan [Land]
40833241	2024-11-15T08:05:45	39.74	15.59	278.2	ML 3.8	North-Western Calabria Coast (Cosenza)
40934471	2024-11-26T13:47:07	36.86	136.5	34.8	Mwp 6.2	Near west coast of Eastern Honsu, Japan
41306612	2025-01-07T01:05:18	28.59	87.43	5.5	Mwp 7	China [Land]
41628322	2025-02-04T13:04:18	36.55	25.73	14.8	Mwp 5.4	Dodecanese Islands, Greece [Sea: Greece]
41649552	2025-02-07T15:19:12	38.49	14.46	17.1	Mw 4.7	Isole Eolie (Messina)
41659142	2025-02-08T23:23:14	17.61	-82.4	9	Mwpd 7.4	North of Honduras [Sea: Honduras]
41663452	2025-02-09T19:05:40	36.51	25.64	19.7	Mwp 5.5	Dodecanese Islands, Greece [Sea: Greece]
41670462	2025-02-10T20:16:30	36.58	25.7	9.2	Mwp 5.4	Dodecanese Islands, Greece [Sea: Greece]

Event ID	Time (UTC)	Latitude N	Longitude E	Depth (km)	Magnitude	Description
41671032	2025-02-10T22:37:27	36.55	25.69	11.5	Mwp 5.4	Dodecanese Islands, Greece [Sea]
41748192	2025-02-18T16:54:34	37.98	21.1	11.5	mb 5.1	Ionian Greek Coast

3.1 The polarization method

In the first method we have exploited the direction of vibration of first arrival P-waves from earthquake recordings. Knowing the geographic station coordinates and the earthquake location, the radial direction is identified by the back-azimuth θ_{baz}, the angular direction from the station to the source, measured clockwise from north. Rotating the horizontal components in the radial and tangential directions, the P-wave has a greater amplitude in the radial component compared to the tangential one, being the compressional body wave P mainly polarized in the vertical and radial direction (Zheng and McMechan, 2006). As the starting direction of the horizontal components of the borehole seismic station is unknown, we rotate both components until a direction θ_{rad} is found, that maximizes the amplitude of the direct P-onset of one of the two components (and minimizes the other, which is perpendicular). The rotation angle θ_{rot} is then:

$$\theta_{rot} = \theta_{rad} = \theta_{baz} \tag{1}$$

The value θ_{rot} is the clockwise rotation of the maximized component (HH1 in our case) to reach the north direction (and of HH2 to reach the east direction). Consequently, the azimuthal directions according to which the components HH1 and HH2 are placed, clockwise from north, are:

$$\theta_{az}(HH1) = 360° - \theta_{rot} \tag{2}$$

$$\theta_{az}(HH2) = 360° - \theta_{rot} + 90° \tag{3}$$

Figure 9 shows the three components recorded by the station OTP1 for the Japanese earthquake listed in Table 2 with ID 39998581.

To find θ_{rad}, we have rotated the first horizontal component (HH1) clockwise of an angle θ, and the second (HH2) perpendicularly to it ($\theta + 90°$). θ ranges from 0° to 180° with a step size of 10°. In Fig. 10 (a) the horizontal components HH1 and HH2 are overlapped in the time window of the direct P-wave, after a rotation of $\theta = 160°$ for HH1 (and $\theta = 250°$ for HH2). In this direction the wave reaches its maximum of amplitude on HH1, and its minimum on HH2. In Fig. 10 (b) the particle motion of the P-wave is shown.

The angle $\theta + 180°$ maximizes HH1 and the two angles perpendicular to θ and $\theta + 180°$, maximize HH2. This ambiguity could be easily resolved by comparing the direct P-wave polarity on the three components of station OTP1 with the reference station OT11. The earthquake has a back-azimuth of 50°, so, considering the vectorial velocity of P-waves, we expect a negative component of the first pulse on the N and E axes and a positive one on the Z axis (or N, E positive and Z negative). As we can see from station OT11 in Fig. 11 (a), the vertical component has a positive first pulse, and horizontal components have a negative first pulse. With the angle $\theta_{rad} = 160°$, results from Eq. (1) that $\theta_{rot} = 110° \pm 5°$ (i.e. the uncertainty is half of the step). This angle leads to a negative first P-pulse on horizontal components of station OTP1, as the reference station OT11. Note that after the rotation, the three components of station OTP1 (Fig. 11b) are very similar to those recorded by the reference station OT11 (Fig. 11a).

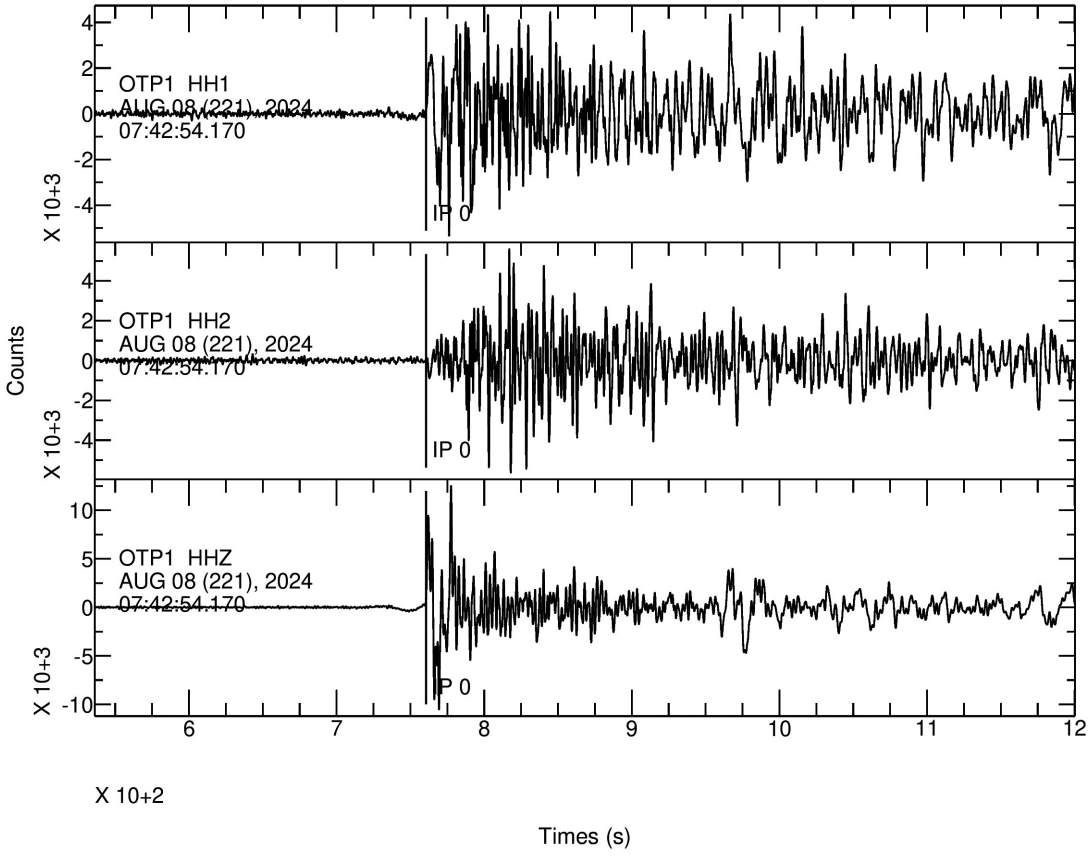

Figure 9. The three components recorded by seismic station OTP1 for the Japanese earthquake. The hypocentres coordinates are in Table 2, ID 39998581.

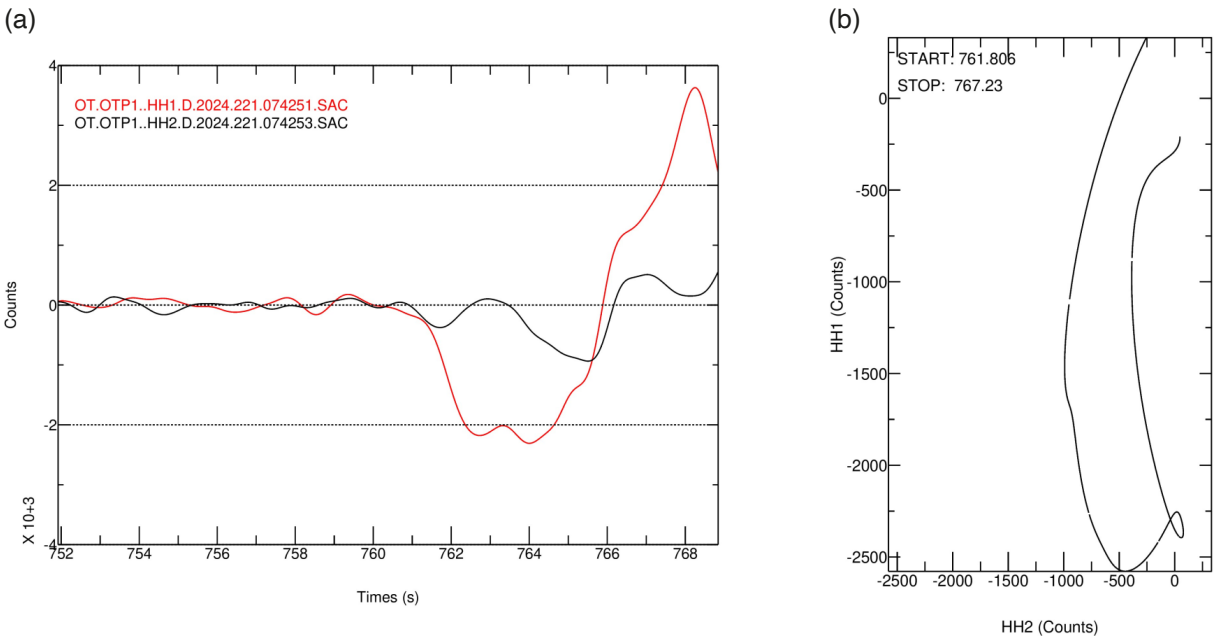

Figure 10. (a) The two horizontal components of station OTP1, overlapped in the time window of the direct P-wave, after rotation of $\theta = 160°$, (b) particle motion; earthquake ID: 39998581.

We have calculated θ_{rot} for all the earthquakes listed in Table 2 and averaged the resulting values. The mean is $\theta_{rot} = 118° \pm 8°$. The calculated mean azimuthal directions of HH1 and HH2, result:

$$\theta_{az}(HH1) = 243° \pm 8° \tag{4}$$

$$\theta_{az}(HH2) = 333° \pm 8° \tag{5}$$

The two values θ_{az} are the azimuthal directions, clockwise from north according to which HH1 and HH2 are placed inside the borehole.

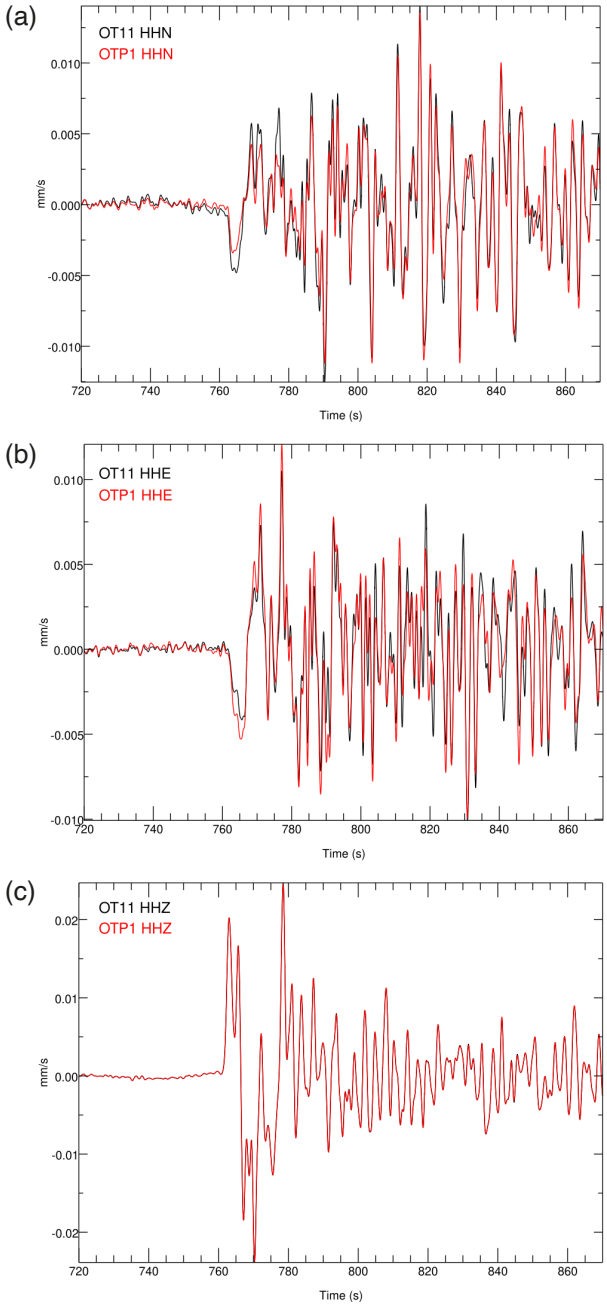

Figure 11. (a) The three components oriented (a) N-S, (b) E-W and (c) vertical of the station OTP1 (red) are overlapped to the corresponding component of OT11 (black) for the Japanese earthquake (earthquake ID: 39998581), after the clockwise rotation of OTP1 horizontal waveforms of $\theta_{rot} = 110°$.

3.2 The correlation analysis

To verify the reliability of the previous estimation, we have also applied a correlation analysis to the same dataset in Table 2 to calculate the direction of horizontal components of OTP1. We have considered the station OT11 (placed at the surface) as a reference station. For OTP1 and OT11 we have assumed the plane-wave approximation, which requires that the distance d between the two sensors is much less than the dominant wavelength λ of the signal $d \ll \lambda$. The signals must be filtered with a cut-off frequency $f_c \ll vd^{-1}$ with v the lowest velocity of the medium. Considering a $v_s \neq 600$ m/s (http://www.otrions.uniba.it/, last accessed on 2025 February, 28) and a distance $d \sim 32$ m between OT11 and OTP1 ($d = \sqrt{10^2 + 30^2}$), $f_c \ll 19$ Hz. We have, therefore, applied a bandpass filter [0.01, 1] Hz to the seismic recordings.

The horizontal components of the post-hole sensor (HH1 and HH2) of the OTP1 station were systematically rotated clockwise from 0° to 360° with 1° step size. In each rotation step, we have computed the Kendall's tau correlation coefficient (Shieh, 1998) between the rotated component of HH1 and the north component of OT11, as well as between the rotated component of HH2 and the east component of OT11. Kendall's Tau (τ) measures the distance between two numerical series by evaluating the degree of concordance between their paired values. It quantifies how similarly the two series are ordered, with values ranging from −1 (complete inverse order) to 1 (perfect agreement), and 0 indicating no correlation. The correlation coefficient is derived here considering the same alignment and time window length for both stations, which starts from origin time and whose ends depend on epicentral distance from 20 to 30 minutes. In the time window, the noise preceding the seismic signal is included.

The azimuth yielding the highest correlation between HH1 (of OTP1) and the north component (of OT11) and HH2 (of OTP1) and the east component (of OT11) corresponds to the optimal azimuthal angle θ_{az}, representing the orientation of the post-hole sensor relative to the surface reference sensor. Finally, the rotated signals of OTP1 have been visually compared with the reference OT11 signals to validate the alignment, using both time-series plots and particle motion plots of the signal components before and after rotation.

The plot in Fig. 12a depicts the variation of τ with θ_{az} calculated from the seismic traces of the Japanese earthquake listed in Table 2 with ID 39998581. For the angle $\theta_{az} = 232°$, the maximum value of $\tau = 0.95$ is found. Figure 12b shows the comparison of the seismic traces of the OT11 and OTP1 stations recorded for the same earthquake. It is worth noting that after the rotation in the computed direction θ_{az}, the horizontal components of OTP1 are identical to those of OT11. The application of the angle $\theta_{az} = 232°$ found with the proposed method produces a correct alignment of the motion of the particles in the horizontal plane for OTP1. The two visual comparisons described and shown confirm that the value of the angle of misalignment between the unknown orientation of the axes of the OTP1 station and the orientation of the axes of the OT11 reference station is correct.

By considering all the earthquakes listed in the Table 2 the average maximum τ is $\tau = 0.91 \pm 0.07$ for:

$$\theta_{az}(HH1) = 232° \pm 0.5° \tag{6}$$

$$\theta_{az}(HH2) = 322° \pm 0.5° \tag{7}$$

Both methodologies applied on seismic recordings show concordant results, although the method based on the maximization of the correlation coefficient shows a more precise value of the angle θ_{az} compared to the value deriving from the polarization analysis, which is slightly different and shows a higher variability from an earthquake to another.

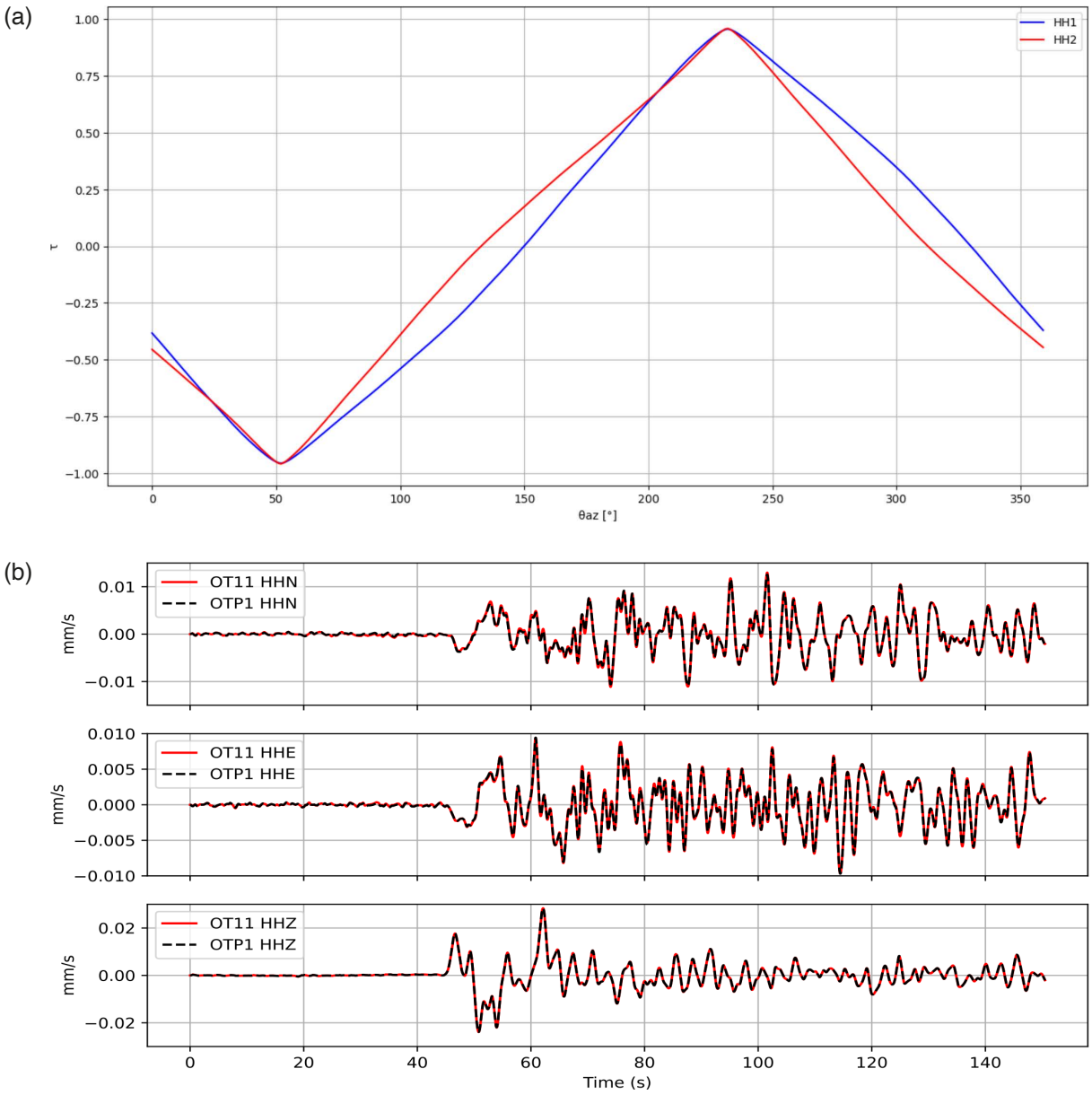

Figure 12. (a) The calculated τ between OT11 and OTP1 at each θ_{az}, calculated for the same seismic event (ID: 39998581) shown in Fig. 11 and listed in Table 2. The graph shows that the maximum correlation is achieved for an azimuth of $\theta_{az} = 232°$. (b) The three components of the station OTP1 (black), oriented N-S, E-W and vertical, are overlapped to the corresponding component of OT11 (red) for the Japanese earthquake (ID: 39998581), after the rotation of OTP1 horizontal waveforms in the direction θ_{az}.

4. PPSDs of the background seismic noise

To check the background seismic noise of the new post-hole seismometer and the upgraded broadband sensors, we have computed the Probabilistic Power Spectral Densities (PPSDs) for the recorded signal. The PPSDs are calculated using the specific function implemented in ObsPy (Krischer et al., 2015), which is based on the algorithm of McNamara and Buland (2004). The PPSDs show the probability of having a certain level of noise at each period of analysis, and the noise is expressed in terms of Power Spectral Density (PSD). We have computed the Probability Density Function (PDF) of the PSD of a continuous 7-days signal, including working days and the weekend.

Figure 13 compares the PPSDs of the surface station OT11 and the co-located borehole station OTP1. The horizontal components of OTP1 (HH1 and HH2), are rotated in the north and east direction, respectively, according to the angle retrieved in the previous paragraph. The vertical colour palette shows the PPSD, whereas the two grey curves are the high-level and low-level noise models of Peterson (1993), which indicate the maximum and minimum acceptable noise levels. The horizontal colour bar below each panel shows the availability of the signal in green, or any gaps in red (first row of the bar), and the considered segment for the calculation of the PPSD in blue (second row of the bar). Both sensors (OTP1 and OT11), have a flat response below 120 s. They have a PPSD near the high-level noise model for periods less than 5 s, but for periods ranging from 0.3 – 1 s OT11 has a PPSD slightly above the high-level noise model. An amelioration for recorded signal by the posthole seismometer is then observed for the influence of the cultural noise, which ranges from 0.03-1 s (Díaz et al., 2017), according to which the noise level is 20 dB smaller. The significant difference, however, regards periods higher than 5 s, since OTP1 records very good signals, with a level of noise 40 dB less than OT11 above this period and shows much more stability in the noise variability with time. In general, the PSD of the borehole station shows a smaller variability during the week at each frequency compared with those recorded by the OT11 station, placed at the surface. In Fig. 14 the PPSDs of upgraded broadband sensors, having a flat response below 20 s, are shown (OT12, OT14, OT16). For the same week of recording in the winter season, the stations OT12 and OT14 show very good, recorded signals, with a noise level between the low-level and high-level noise models of Peterson (1993), whereas the station OT16 has a PPSD near the high-level noise model, especially in the period range of 0.2-3 s. These stations are installed near the coast and show a similar shape of the PPSD curves.

Regarding the station OT05, as we mentioned in Section 2, the cabin is equipped with a cooling fan as it is exposed to the sun all day. So, we evaluated whether the cooling system can add some noise source to the recordings. We chose to calculate the PPSDs by selecting a week in daytime hours (8-20) in July, to be sure that the cooling system is on (Fig. 15a, c and e), and a week of recordings in nighttime hours (20-8) in December, to be sure that the cooling system is off (Fig. 15b, d and f). The results reported in Fig. 15 do not highlight any differences in any period between winter and summer, as the noise level is approximately near (and below) –140 dB in, for all frequencies. The cooling system, therefore, does not affect the recordings.

All the stations show a peak in the PPSDs at periods of 2-3 s. The station OT11, near Lucera shows the highest noise level for each period, among the upgraded broadband seismic sites. The station OT05, installed near the small city of Rignano Garganico in the foreland of GP, shows the smallest noise level for periods smaller than 10 s. The latter are influenced by local-scale meteorological conditions and noise induced by human activity. At periods greater than 10 s, the minimum values of PSD curves are exhibited by the posthole sensor, OTP1.

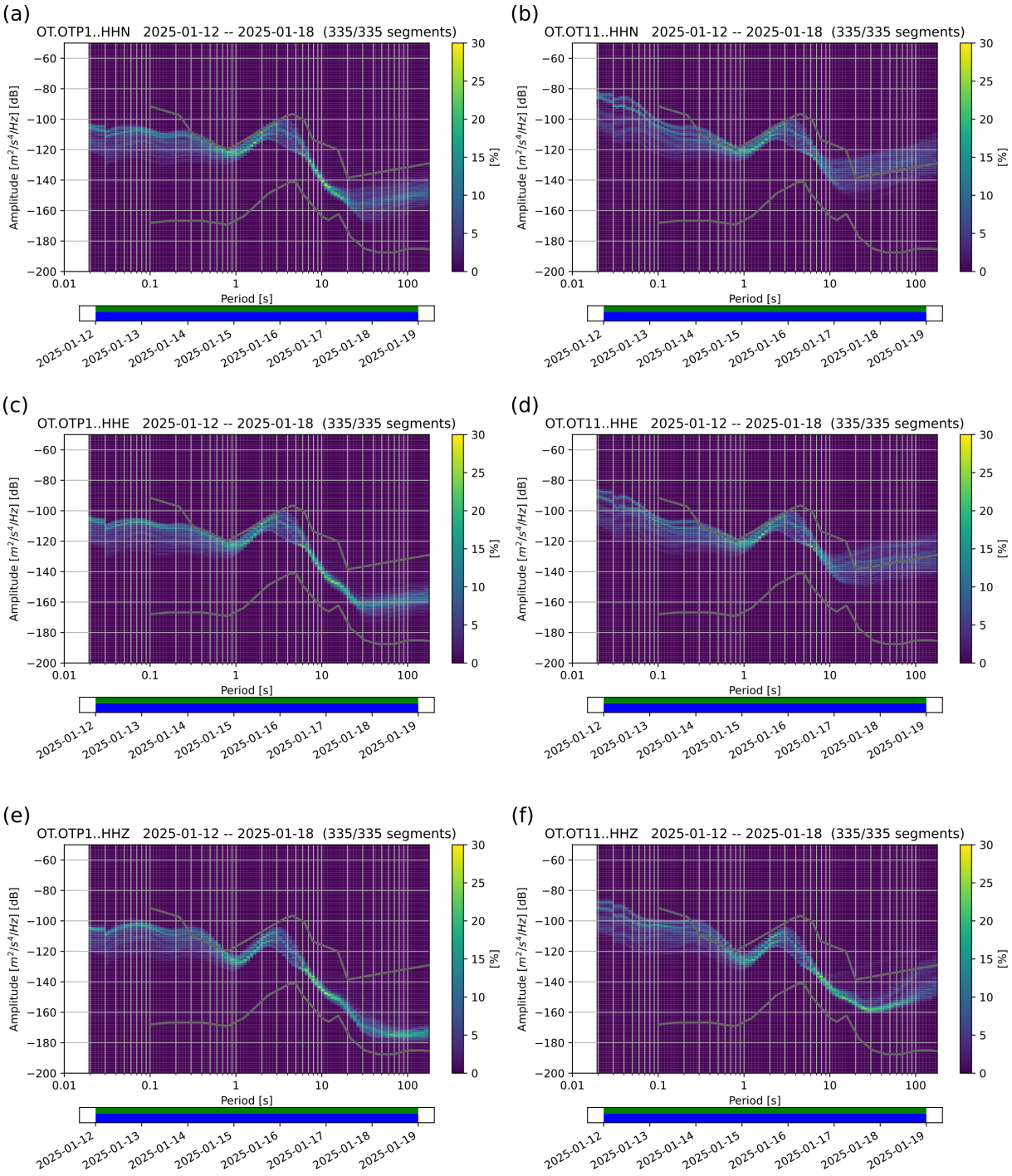

Figure 13. PPSDs of the three components of the seismic stations OTP1 and the upgraded broadband OT11. The title contains the name and the component of the station, and the week considered for the calculation. The vertical colour bar on the right shows the PDF of the PSD for different periods. The horizontal bar shows the availability of the signal (first row, green) or the gaps (first row, red) and the signal segment to calculate the PPSD (second row, blue).

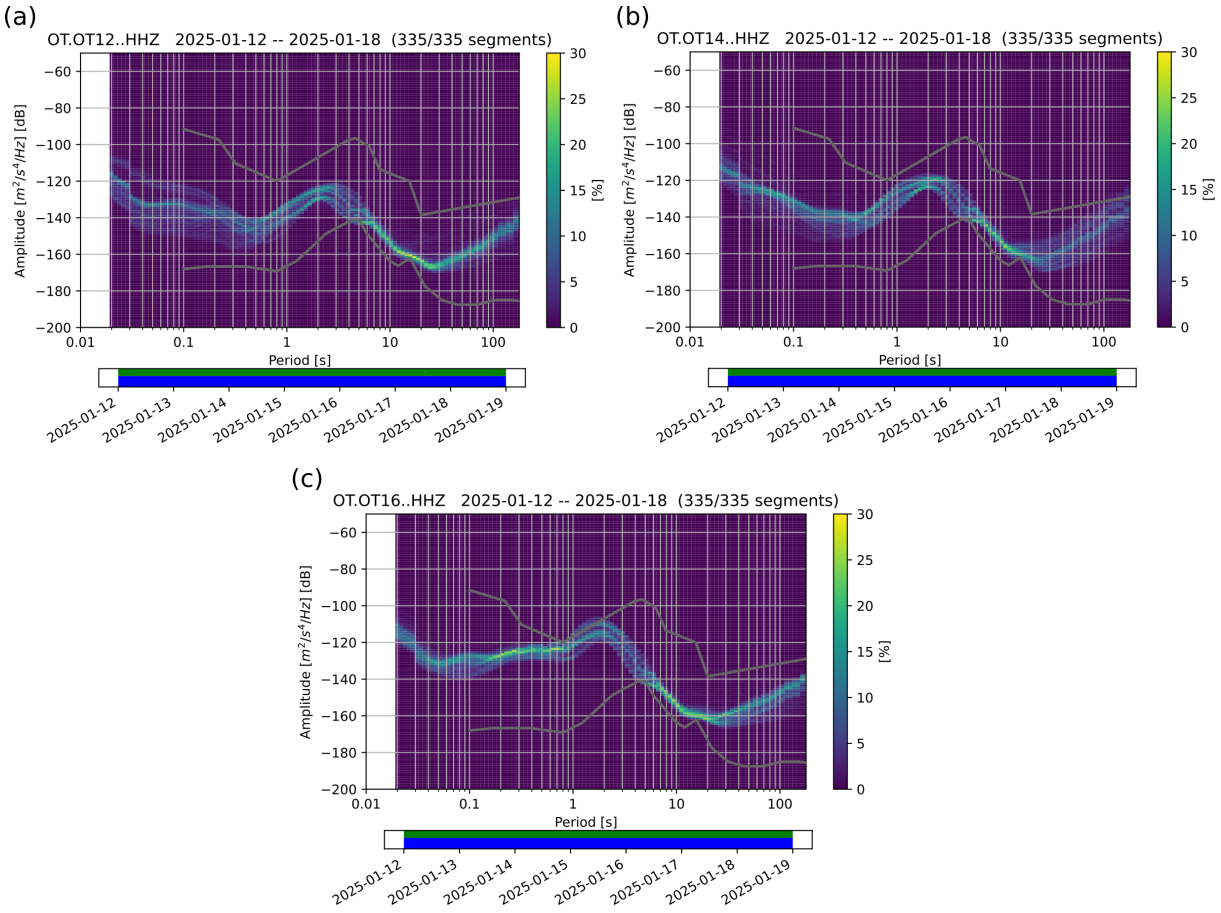

Figure 14. PPSDs of vertical components recorded by upgraded broadband seismic stations: (a) OT12; (b) OT14; (c) OT16. The title contains the name and the station component, and the week considered for the calculation. The vertical colour bar on the right shows the PDF of the PSD for different periods. The horizontal bar shows the availability of the signal (first row, green) or the gaps (first row, red) and the signal segment to calculate the PPSD (second row, blue).

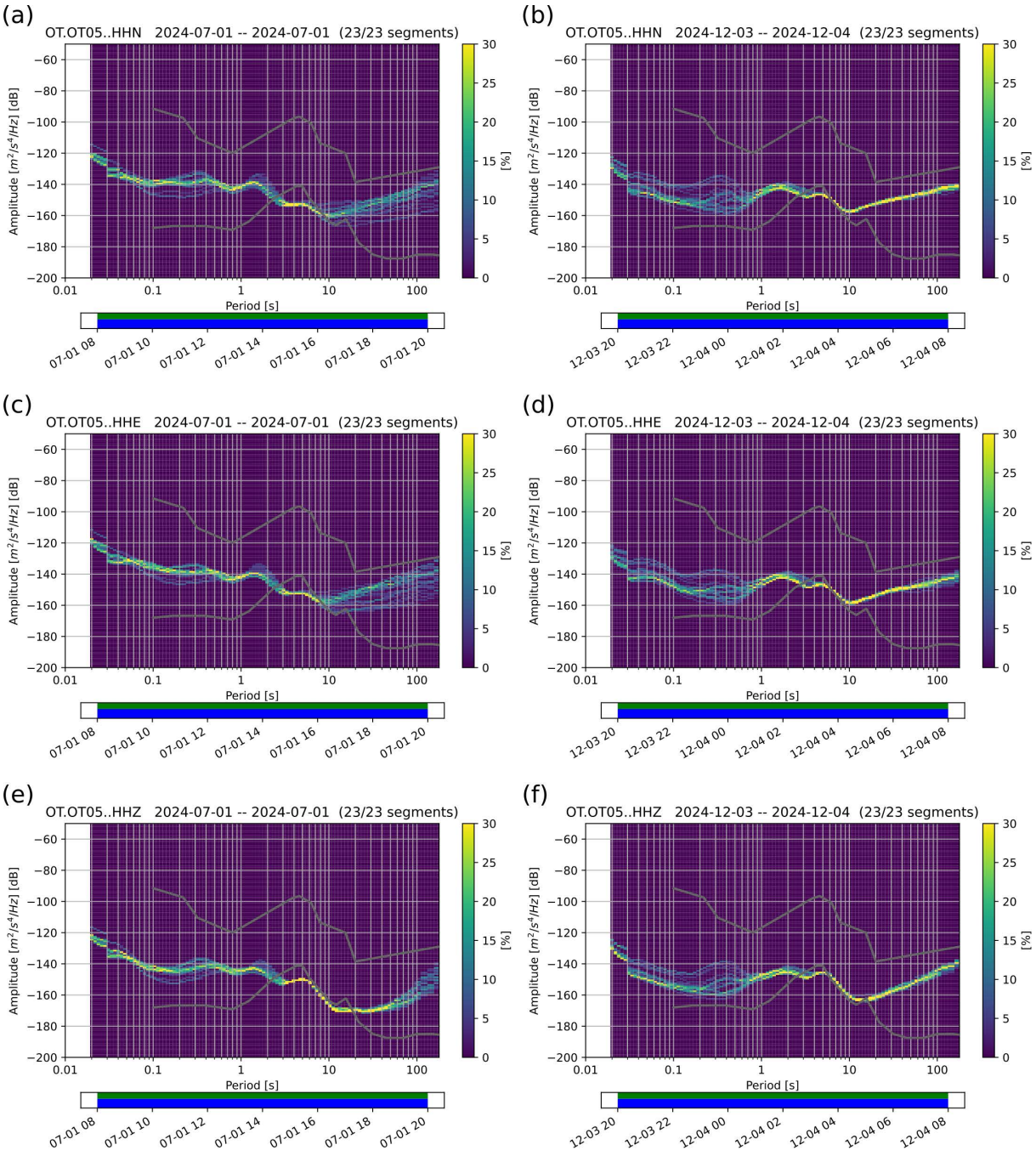

Figure 15. PPSDs of the three components of station OT05, computed with 12h signals recorded during daylight in summer (a), (c), (e) and during the nighttime in winter (b), (d), (f). The title contains the name and the component of the station, and the day considered for the calculation. The vertical colour bar on the right shows the PDF of the PSD for different periods. The horizontal bar shows the availability of the signal (first row, green) or the gaps (first row, red) and the signal segment to calculate the PPSD (second row, blue).

5. Discussion and conclusion

In this article, we have shown the updating details of some seismic stations of OT network and the installation phases of a posthole seismometer in a 30 m deep well.

We upgraded six out of the twelve short period stations of the OT network with broadband seismometers. Table 1 shows details of instruments and operation time of OT network. We considered and described many different aspects of the design phase to perform a masterly installation of the post-hole seismometer.

We have estimated the direction θ_{az} of the horizontal components of OTP1 comparing them with the N and the E components of the reference station OT11, placed in the same location of OTP1, at the surface. We have computed the angle θ_{az} applying two methods: the first based on the polarization of direct P-waves and the second based on the maximization of the correlation coefficient between OTP1 and OT11. The polarisation analysis gives the angle $\theta_{az} = 243° \pm 8°$ (clockwise rotation from N) for HH1 component of OTP1 and $\theta_{az} = 333° \pm 8°$ for the HH2 component, since HH1 and HH2 are perpendicular. The value of θ_{az} computed with the correlation-based method instead is $\theta_{az} = 232° \pm 0.5°$ for HH1 component and $\theta_{az} = 322° \pm 0.5°$ for HH2. The resulting values from both methods are comparable.

The polarization analysis requires an excellent signal-to-noise ratio for the first P-wave onset, searching the direction that maximizes the amplitude of P-wave in the radial component. There is also a tangential component of the P-wave due to the lateral heterogeneity of the medium crossed by waves resulting in a not well-defined maximum of amplitude in the radial direction. Moreover, it is also necessary to consider the error of the earthquake location, which affects the back-azimuth direction. For these reasons, the estimate resulting from the polarization analysis differs from one earthquake to another, showing more variability compared to the value resulting from the correlation analysis.

The correlation-based method assumes a correct orientation of the reference station. We can be confident on this assumption, as we have recently installed the new sensor for the reference station OT11, correctly orienting all the three components. This method is more flexible as it can be applied to background noise or to earthquake recordings, even if these are not of good quality.

For all these reasons, we have decided to indicate:

$$\theta_{az}(HH1) = 232° \tag{8}$$

$$\theta_{az}(HH2) = 322° \tag{9}$$

as optimal orientation of the post-hole seismometer OTP1. These values can be found at the station web page https://terremoti.ingv.it/en/instruments/station/OTP1 (accessed on 11th June 2025).

The geographical distribution of the newly installed broadband sensors has been strategically chosen to cover the entire GP region (see Fig. 1). With the future substitutions of the short-period sensors, the broadband sensors of the OT network will become denser, and the OT detection capability will furtherly increase. We have computed the PPSDs of the new broadband seismometers and the posthole sensor OTP1. All the PPSDs show an acceptable noise level, always between the high-level and low-level noise models of Peterson (1993) and between the models retrieved for the Italian territory by D'Alessandro et al. (2021). The PPSDs clearly show the "secondary micro-seismic peak" at periods of 2-3 s. This peak is normally in the period range of 0.8-8 s and has been mainly related to the local effects of wind and sea (e.g. Tsai and McNamara, 2011). The PPSDs of the stations OT12, OT14, OT16, installed near the coast, have the value of this peak comparable with those retrieved for the IV stations (Istituto Nazionale di Geofisica e Vulcanologia, 2005). The latter are installed near the coast of the Adriatic Sea (D'Alessandro et al., 2021) and they have a period comparable with those of the microseisms generated by storms over the Mediterranean Sea, especially in winter season (Marzorati and Bindi, 2006). The station OT05, installed in the hinterland, shows a smaller peak, as expected. The detectable frequency range and the quality of signals increase in the site of Lucera OTP1) thanks to the installation of the posthole sensor, which is less affected by noise from human activity and weather conditions. The posthole sensor shows smaller variability and smaller values of the PSD at all frequency with respect the surface sensor in the same week of recordings. This observation indicates that the station OTP1 is less affected by superficial noise sources, either anthropogenic or environmental. At periods greater than 10 s, the Earth motion caused by local fluctuation in the atmospheric pressure field affects mostly the horizontal components of surface sensors (Sorrells, 1971; Sorrels et al., 1971) as shown by the station OT11, having more variability in the noise level with time, compared with the posthole station OTP1. The deformation associated with pressure changes are attenuated with depth (Peterson, 1993) and the borehole sensor could contribute to improve the long-periods signals recorded in this site. In the Po plain basin, it has been observed that a borehole installation is able to detect many more earthquakes that are hidden by the noise level in the surface sensor (Cocco et al., 2001).

We have considered the SNR of the recorded signals to compute the orientation angle of OTP1. We have observed that the seismograms recorded by the OT11 have a lower SNR than that recorded by the borehole station OTP1. It is worth noting that we have analysed the largest earthquakes with good signals. Smaller earthquakes, consequently, may be hidden by the noise of OT11. The noise level is depth-dependent (Hutt et al., 2017) and it has been observed that the signal to noise ratio increases with depth (Rossi et al., 2023). The borehole sensor could, therefore, contribute to detect the micro-seismicity of the area (Lai et al., 2022), as the background seismic noise is lower at this station for periods smaller than 1 s. The estimated noise reduction observed between the surface station OT11 and the borehole station OTP1 in the Tavoliere plain is encouraging and supports the relevance of the installation. The borehole station is even more valuable considering that the site of Lucera shows, for all periods, the highest values of the noise in the PSD, compared to the other sites in which we have installed the broadband sensors.

The recordings of the OT network stations have been used in recent years to carry out active crustal tectonics studies on the GP which will be expanded with the forthcoming upgrading of the seismic stations.

Earthquakes recorded by OT network shows a peculiar seismogenic layer located in the lower crust that deepens from SW to NE (Filippucci et al., 2021; Ferreri et al., 2025). GP deformation is accommodated by revers to strike slip focal mechanisms (Miccolis et al., 2021), in agreement with the Italian stress map (Montone and Mariucci, 2016). Seismic attenuation tomography with Q coda methods confirms the presence of a high-Q zone in the shallow crust and a low-Q zone where deep seismicity is located (Filippucci et al., 2021b). A thermo-rheological model recently presented (Lavecchia et al., 2022) interprets the lower crust seismicity as due to the rise of deep mantle fluids that lubricate the brittle/ductile transition zone in the lower crust. To correlate the peculiar seismicity distribution with seismic discontinuities and with the presence of fluids, the study of the crust structure and of v_P/v_S profiles is in progress through the receiver function analysis of teleseismic events. The newly installed broadband seismic stations represent a significant integration to the analysed dataset for this ongoing study. Particularly valuable will be data recorded by station OT11, which is the only OT station located in the foredeep of this area, between the Apennines and the foreland (the GP). This represents a fundamental point of measurement to determine crustal thickness and velocity profile in this geological domain. Further studies are oriented to the calculation of a calibration function to compute the local magnitude for the GP area and to build a new seismic catalogue using PhaseNet as a seismic detector (Zhu and Beroza, 2019; Ferreri et al., in preparation). Since 2019 data recorded by OT network are available on EIDA archive (https://eida.ingv.it/it/network/OT, accessed 04/06/2025). These data are currently used by the ONT (Osservatorio Nazionale Terremoti, https://www.ont.ingv.it/, accessed 04/06/2025) for seismic surveillance purposes of the Italian territory. The renewal of the instrumentation described in this paper, therefore, has also the aim of contributing the expansion of the National Seismic Network and satisfying its standards (https://www.ingv.it/en/monitoraggio-e-infrastrutture/reti-di-monitoraggio/l-ingv-e-le-sue-reti/rns, accessed 04/06/2025).

The University of Bari, with the OT network, as well as dealing with research, responds also to the mission of education and relations with the territory. The OT network is used for teaching purposes within the Bachelor, and master's degrees and PhD courses provided by University of Bari. Its seismic laboratories host specific software as the SeisComPRO, the professional version of SeisComP3 developed by GFZ and Gempa GmbH (2008), and CASP, the Complete Automatic Seismic Processor developed by Scafidi et al. (2019), both used for data archiving, automatic detection and earthquake localization. Since 2013, University of Bari and INGV have joined their efforts for the renewal and the maintenance of the OT seismic network in the GP. This is the most seismically active region of Apulia, as shown by historical (e.g. Rovida et al., 2020) and new earthquake catalogues, and deserves continuous seismic monitoring and upgrading of the instrumentation, to carry out new studies.

Data availability statement.

- Seismograms can be downloaded at: https://orfeus-eu.org/webdc3/
- Metadata and information on OT network can be downloaded at: https://terremoti.ingv.it/en/instruments/network/OT
- The earthquakes list used in this study can be requested at this address: https://terremoti.ingv.it/
- Plots were made using SAC (Seismic Analysis Code, Goldstein et al., 2003; Goldstein and Snoke, 2005), the Obspy tool (Beyreuther et al., 2010), the PyGMT tool (Tian et al., 2023).

Acknowledgements. We would like to thank: Rossella Giannuzzi, Ciriaco D'Ambrosio, Annalisa Romeo for the support during the OTP1 design and installation and Salvatore Mazza for the support for data analysis.
MEET Project (Monitoring Earth's Evolution and Tectonics) in the framework of National Recovery and Resilience

Plan (PNRR) – Mission 4, "Education and Research" – Component 2, "From research to business" – Investment line 3.1, "Fund for the creation of an integrated system of research and innovation infrastructures" – project code IR0000025.
GRINT Project Italian Research Infrastructure for Geosciences (Geoscience Research INfracstructure of ITaly; GRINT; project code PIR01_00013), National Operational Programme (PON) in implementation of Action II.1 of the PON Research and Innovation 2014-2020".
RETURN Project (Multi-Risk science for resilient commUnities undeR a changiNg climate) Extended Partnership in the framework of European Union – NextGenerationEU (National Recovery and Resilience Plan – NRRP, Mission 4, Component 2, Investment 1.3 – D.D. 1243 2/8/2022, PE0000005).

References

Amato, A., I. Bianchi and N. P. Agostinetti (2014). Apulian crust: Top to bottom, J. Geodyn., 82, 125-137, doi:10.1016/j.jog.2014.09.007.

Aster, R. C. and P. M. Shearer (1991). High-frequency borehole seismograms recorded in the San Jacinto Fault zone, Southern California Part 2, Attenuation and site effects, Bull. Seismol. Soc. Am., 81, 4, 1081-1100, doi:10.1785/BSSA0810041057.

Beyreuther, M., R. Bertsch, L. Krischer, T. Megies et al. (2010). ObsPy: A Python Toolbox for Seismology, Seismol. Res. Lett., 81, 3, 530-533, doi:10.1785/gssrl.81.3.530.

Casnedi, R. (1988). La fossa Bradanica: origine, sedimentazione e migrazione, Mem. Soc. Geol. Ital., 41, 439-448, http://pascal-francis.inist.fr/vibad/index.php?action=getRecordDetail&idt=6371714.

Cocco, M., F. Ardizzoni, R. M. Azzara, L. Dall'Olio et al. (2001). Broadband waveforms and site effects at a borehole seismometer in the Po alluvial basin (Italy), Ann. Geophys., 44, 1, doi:10.4401/ag-3611.

D'Alessandro, A., L. Greco, S. Scudero and V. Lauciani (2021). Spectral characterization and spatiotemporal variability of the background seismic noise in Italy, Earth Space Sci., 8, e2020EA001579, doi:10.1029/2020EA001579.

Del Gaudio, V., P. Pierri, A. Frepoli, G. Calcagnile et al. (2007). A critical revision of the seismicity of Northern Apulia (Adriatic microplate – Southern Italy) and implications for the identification of seismogenic structures, Tectonophysics, 436, 9-35, doi:10.1016/j.tecto.2007.02.013.

Díaz, J., M. Ruiz, P. S. Sánchez-Pastor and P. Romero (2017). Urban seismology: On the origin of earth vibrations within a city, Sci. Rep., 7, 1, 1-11, doi:10.1038/s41598-017-15499-y.

Di Bucci, D. and S. Mazzoli (2002). Active tectonics of the Northern Apennines and Adria geodynamics: new data and a discussion, J. Geodyn., 34, 5, 687-707, doi:10.1016/S0264-3707(02)00107-2.

Ekström, G. and R. W. Busby (2008). Measurements of seismometer orientation at USArray transportable array and backbone stations, Seismol. Res. Lett., 79, 4, 554-561, doi:10.1785/gssrl.79.4.554.

Ferreri, A. P., A. Romeo, R. Giannuzzi, T. Ninivaggi et al. (2025). The new seismic catalog of the Gargano area (Southern Italy) after a decade of seismic monitoring by OTRIONS network, Mendeley Data, 2, doi:10.17632/nhfvx7ysxw.2

Filippucci, M., S. Miccolis, A. Castagnozzi, G. Cecere et al. (2021). Seismicity of the Gargano promontory (Southern Italy) after 7 years of local seismic network operation: Data release of waveforms from 2013 to 2018, Data in brief, 35, 106783, doi:10.1016/j.dib.2021.106783.

Filippucci, M., S. Lucente, E. Del Pezzo, S. de Lorenzo et al. (2021b). 3D-Kernel based imaging of an improved estimation of (Qc) in the Northern Apulia (Southern Italy), Appl. Sci., 11, 16, 7512, doi:10.3390/app11167512.

Goldstein, P., D. Dodge, M. Firpo and L. Minner (2003). SAC2000: Signal processing and analysis tools for seismologists and engineers, in Invited contribution to The IASPEI International Handbook of Earthquake and Engineering Seismology A. Lee, W. H. K., H. Kanamori, P. C. Jennings et al. (Eds.), Accademic Press, London, 1613-1614, doi:10.1016/S0074-6142(03)80284-X.

Goldstein, P. and A. Snoke (2005). SAC Availability for the IRIS Community, Incorporated Institutions for Seismology Data Management Center Electronic Newsletter.

Helmholtz Centre Potsdam GFZ, German Research Centre for Geosciences and Gempa GmbH (2008). The SeisComP seismological software package, GFZ Data Services, doi:10.5880/GFZ.2.4.2020.003.

Hutt, C. R., A. T. Ringler and L. S. Gee (2017). Broadband Seismic Noise Attenuation versus Depth at the Albuquerque Seismological Laboratory, Bull. Seismol. Soc. Am., 107, 3, 1402-1412, doi:10.1785/0120160187.

Istituto Nazionale di Geofisica e Vulcanologia INGV (2005). Rete Sismica Nazionale RSN, Data set, Istituto Nazionale di Geofisica e Vulcanologia INGV, doi:10.13127/SD/X0FXNH7QFY.

Krischer, L., T. Megies, R. Barsch, M. Beyreuther et al. (2015). ObsPy: a bridge for seismology into the scientific Python ecosystem, Comput. Sci. Discovery, 8, 014003, doi:10.1088/1749-4699/8/1/014003.

Lai, T. S., W. A. Chao and Y. M. Wu (2022). A local magnitude scale from borehole recordings with site correction of the surface to downhole, Seismol. Res. Lett., 93, 3, 1524-1531, doi:10.1785/0220210252.

Lavecchia, A., M. Filippucci, A. Tallarico, G. Selvaggi et al. (2022). Role of crustal fluids and thermo-mechanical structure for lower crustal seismicity: The Gargano Promontory (Southern Italy), Glob. Planet. Change, 217, 103929, doi:10.1016/j.gloplacha.2022.103929.

Marzorati, S. and D. Bindi (2006). Ambient noise levels in North Central Italy, Geochem. Geophys. Geosyst., 7, 9, doi:10.1029/2006GC001256.

McNamara, D. E. and R. P Buland (2004). Ambient noise levels in the continental United States, Bull. Seismol. Soc. Am., 94, 1517-1527, doi:10.1785/012003001.

Miccolis, S., M. Filippucci, S. De Lorenzo, A. Frepoli et al. (2021). Seismogenic structure orientation and stress field of the Gargano promontory (Southern Italy) from microseismicity analysis, Front. Earth Sci., 9, 589332, doi:10.3389/feart.2021.589332.

Montone, P. and M. T. Mariucci (2016). The new release of the Italian contemporary stress map, Geophys. J. Int., 205, 3, 1525-1531, doi:10.1093/gji/ggw100.

Di Nunno, F. and F. Granata (2020). Groundwater level prediction in Apulia region (Southern Italy) using NARX neural network, Environ. Res., 190, 110062, doi:10.1016/j.envres.2020.110062.

Patacca, E. and P. Scandone (2004). The 1627 Gargano earthquake (Southern Italy): identification and characterization of the causative fault, J. Seismol., 8, 259-273, doi:10.1023/B:JOSE.0000021393.77543.1e.

Peterson, J. (1993). Observations and Modeling of Seismic Background Noise, U. S. Geol. Surv. Open File Rep., 93-322, doi:10.3133/ofr93322.

Pieri, P., V. Festa, M. Moretti and M. Tropeano (1997). Quaternary tectonic activity of the Murge area (Apulian foreland – Southern Italy), Ann. Geophys., 40, 5, 1395-1404, doi:10.4401/ag-3876.

Ricchetti, G., N. Ciaranfi, E. Luperto Sinni, F. Mongelli et al. (1988). Geodinamica ed evoluzione sedimentaria dell'Avampaese Apulo, Mem. Soc. Geol. Ital., 41, 57-82.

Rossi, C., F. Grigoli, P. Gasperini, S. Gandolfi et al. (2023). Seismic noise reduction as a function of depth recorded by a vertical array installed in a 285-m-deep borehole at a gas storage field in Northern Italy, Seismol. Res. Lett., 94, 4, 1925-1935, doi:10.1785/0220220337.

Rovida, A., M. Locati, R. Camassi, B. Lolli et al. (2020). The Italian earthquake catalogue CPTI15, Bull. Earth. Eng., 18, 7, 2953-2984, doi:10.1007/s10518-020-00818-y.

Scafidi, D., D. Spallarossa, G. Ferretti and S. Barani (2019). A complete automatic procedure to compile reliable seismic catalogs and travel-time and strong-motion parameters datasets, Seismol. Res. Lett., 90, 3, 1308-1317, doi:10.1785/0220180257.

Shieh, G. S. (1998). A weighted Kendall's tau statistic, Stat. Probab. Lett., 39, 1, 17-24, doi:10.1016/s0167-7152(98)00006-6.

Sorrells, G. G. (1971). A preliminary investigation into the relationship between long-period seismic noise and local fluctuations in the atmospheric pressure field, Geophys. J. Int., 26, 1-4, 71-82, doi:10.1111/j.1365-246X.1971.tb03383.x.

Sorrells, G. G., J. A. McDonald, Z. A. Der and E. Herrin (1971). Earth motion caused by local atmospheric pressure changes, Geophys. J. Int., 26, 1-4, 83-98, doi:10.1111/j.1365-246X.1971.tb03384.x.

Stabile, T. A., V. Serlenga, C. Satriano, M. Romanelli et al. (2020). The INSIEME seismic network: a research infrastructure for studying induced seismicity in the High Agri Valley (Southern Italy), Earth Syst. Sci. Data, 12, 1, 519-538, doi:10.5194/essd-12-519-2020.

Tallarico, A. (2015). Rete multi-parametrica per lo studio e il monitoraggio dei rischi naturali nel canale d'Otranto e nel Mar Ionio, Ragusa Service, ISBN:9788890670763.

Tian, D., L. Uieda, W. J. Leong, W. Schlitzer et al. (2023). PyGMT: A Python interface for the Generic Mapping Tools, Dataset, Zenodo, doi:10.5281/zenodo.8303186.

Tsai, V. C. and D. E. McNamara (2011). Quantifying the influence of sea ice on ocean microseism using observations from the Bering Sea, Alaska, Geophys. Res. Lett., 38, 22, doi:10.1029/2011gl049791.

University of Bari Aldo Moro (2013). OTRIONS, Data set, International Federation of Digital Seismograph Networks, doi:10.7914/SN/OT.

Ventola, I., M. Balasco, M. De Girolamo, L. Falco et al. (2024). Seismic-electromagnetic signals from two monitoring stations in Southern Italy: Electromagnetic time series release, Geosci. Data J., 11, 4, 863-872, doi:10.1002/gdj3.262.

Wirth, E., A. Vidale, J. E. Frankel, A. D. Pratt et al. (2019). Source-dependent amplification of earthquake ground motions in deep sedimentary basins, Geophys. Res. Lett., 46, 6443-6450, doi:10.1029/2019GL082474.

Zha, Y., S. C. Webb and W. Menke (2013). Determining the orientations of ocean bottom seismometers using ambient noise correlation, Geophys. Res. Lett., 40, 14, 3585-3590, doi:10.1002/grl.50698.

Zhu, W. and G. C. Beroza (2019). PhaseNet: a deep-neural-network-based seismic arrival-time picking method, Geophys. J. Int., 216, 1, 261-273, doi:10.1093/gji/ggy423.

Zeng, X. and G. A. McMechan (2006). Two methods for determining geophone orientations from VSP data, Geophysics, 71, 4, V87-V97, doi:10.1190/1.2208935.

***CORRESPONDING AUTHOR: Teresa NINIVAGGI**,
Istituto Nazionale di Geofisica e Vulcanologia, Sezione Irpinia, Grottaminarda, Italy
e-mail: teresa.ninivaggi@ingv.it